Solar Phys
DOI 10.1007/s11207-013-0465-7

Interplanetary Coronal Mass Ejections, Associated Features, and Transient Modulation of Galactic Cosmic Rays

Anand Kumar · Badruddin

Received: 16 December 2012 / Accepted: 18 December 2013

Abstract Interplanetary structures such as shocks, sheaths, interplanetary counterparts of coronal mass ejections (ICMEs), magnetic clouds, and corotating interaction regions (CIRs) are of special interest for the study of the transient modulation of galactic cosmic rays (GCRs). These structures modulate the GCR intensity with varying amplitudes and recovery-time profiles. It is known that ICMEs are mainly responsible for Forbush decreases in the GCR intensity. However, not all of the ICMEs produce such decreases in GCR intensity. We utilize GCR intensity data recorded by neutron monitors and solar-wind plasma/field data during the passage of ICMEs with different features and structures, and we perform a superposed-epoch analysis of the data. We also adopt the best-fit approach with suitable functions to interpret the observed similarities and differences in various parameters. Using the GCR-effectiveness as a measure of the cosmic-ray response to the passage of ICMEs, about half of the ICMEs identified during 1996 – 2009 are found to produce moderate to very large intensity depressions in GCR intensity. The ICMEs associated with halo CMEs, magnetic-cloud (MC) structures, bidirectional superthermal electron (BDE) signatures, and those driving shocks are 1.5 to 4 times more GCR effective than the ICMEs not associated with these structures/features. Further, the characteristic recovery time of GCR intensity due to shock/BDE/MC/halo-CME-associated ICMEs is larger than those due to ICMEs not associated with these structures/features.

Keywords Galactic cosmic rays · Solar modulation · Forbush decrease · Coronal mass ejection

1. Introduction

In the heliosphere, the large-scale structure of the solar wind is dominated by two types of interplanetary disturbances: transient and corotating disturbances. Corotating disturbances, associated with spatial variability and solar rotation, occur in response to the interaction of

A. Kumar · Badruddin (✉)
Department of Physics, Aligarh Muslim University, Aligarh 202 002, India
e-mail: badr.physamu@gmail.com

Published online: 28 January 2014

fast and slow solar winds. Transient disturbances, due to episodic solar eruptions, expand outward from the Sun into interplanetary space (Gosling, 1996).

The galactic cosmic-ray (GCR) intensity is modulated by long-term effects such as the $\approx$11-year solar-activity cycle and the $\approx$22 year solar magnetic cycle as well as by short-term effects such as the passage of corotating flows (high-speed streams) and transient disturbances (*e.g.* interplanetary coronal mass ejections). Recurrent depressions in GCR intensity due to corotating fields and flows and Forbush decreases due to transient disturbances have been studied in the past (see, *e.g.*, Lockwood, 1971; Rao, 1972; Iucci *et al.*, 1989; Venkatesan and Badruddin, 1990; Cane, 2000; Kudela *et al.*, 2000; Gupta and Badruddin, 2009; Oh and Yi, 2009; Kane, 2010; Wawrzynczak and Alania, 2010; Abbrescia *et al.*, 2011; Modzelewska and Alania, 2012; Sabbah and Kudela, 2012, and references therein).

Short-term transient depressions caused generally by ICMEs and particularly by magnetic clouds have been studied extensively and many features of the resulting depressions in GCR intensity, including their recovery characteristics, have been clarified (see, *e.g.* Badruddin, Yadav, and Yadav, 1986; Zhang and Burlaga, 1988; Nagashima *et al.*, 1990; Kahler and Reames, 1991; Lockwood, Webber, and Debrunner, 1991; Cane, 1993; Mavromichalaki *et al.*, 2003; Dorotovic *et al.*, 2008; Usoskin *et al.*, 2008; Richardson and Cane, 2011, and references therein). However, important features of fields and flows, their magnetic structure, and the physical processes playing the dominant role are yet to be clearly identified (see, *e.g.*, Jordan *et al.*, 2011; Richardson and Cane, 2011; Dumbovic *et al.*, 2012; Kudela, 2012).

Forbush decreases are characterized by a rapid reduction in cosmic-ray intensity within one to two days followed by a slow recovery typically lasting several days. After their discovery (Forbush, 1937), the search began for their solar sources, responsible interplanetary structures, and physical mechanisms playing an important role. Simpson (1954) related these decreases to solar activity, and individual decreases were generally attributed to solar flares before the beginning of space age or even after (see reviews: *e.g.* Lockwood, 1971; Venkatesan and Badruddin, 1990). However, with the advent of space coronagraphs in the 1970s and subsequent observations of coronal mass ejections (CMEs) and their interplanetary counterparts (ICMEs), it was realized that CMEs instead of solar flares may be the solar cause of Forbush decreases. It is known that only some of the observed ICMEs produce the Forbush decrease in GCR intensity. Cane (2000) states that the maximum of the depression is about 25 % for neutron monitors.

ICMEs with speed from about 300 $\mathrm{km\,s^{-1}}$ up to about 1000 $\mathrm{km\,s^{-1}}$ have been observed. The field enhancements in the ICMEs may have values from a few nT up to about 40 nT (Richardson and Cane, 2010). It is also observed that ICMEs observed in near-Earth space may or may not be associated with shock/sheath (Cane and Richardson, 2003), bidirectional superthermal electron events (Gosling *et al.*, 1987), and magnetic-cloud structures (Gosling, 1990; Richardson and Cane, 2010). Furthermore, the CMEs may have halo structure or not (*e.g.* Gopalswamy, Yashiro, and Akiyama, 2007), where halo CMEs are those with an apparent width of 360 degrees. In this work, we analyze the ground-based neutron-monitor data together with the interplanetary plasma and field data during the passage of ICMEs associated with different features and structures in interplanetary space.

Burlaga *et al.* (1981) and Klein and Burlaga (1982) identified magnetic clouds, a subset of CMEs, in the interplanetary plasma and field data obtained from space-based observations. Subsequently, the role of magnetic clouds and their associated structures (shock/sheath) in producing Forbush decreases were studied extensively (*e.g.* Badruddin *et al.*, 1985; Badruddin, Yadav, and Yadav, 1986; Zhang and Burlaga, 1988; Iucci *et al.*, 1989; Badruddin, Venkatesan, and Zhu, 1991; Lepping *et al.*, 1991; Lockwood, Webber, and Debrunner,

1991; Venkatesan *et al.*, 1992; Ananth and Venkatesan, 1993; Cane, 1993; Cane, Richardson, and von Rosenvinge, 1996; Cane, Richardson, and Wibberenz, 1997). These and many other such studies have lead to the suggestion that ICMEs cause Forbush decreases (Cane, 2000). Subsequent studies of the effect of ICME-related interplanetary disturbances on cosmic rays (*e.g.* Badruddin, 2002; Singh and Badruddin, 2007; Quenby *et al.*, 2008; Subramanian *et al.*, 2009; Yu *et al.*, 2010; Jordan *et al.*, 2011; Richardson and Cane, 2011; Dumbovic *et al.*, 2011, 2012; Augusto *et al.*, 2012; Oh and Yi, 2012; Babu *et al.*, 2013; Blanco *et al.*, 2013) have utilized solar, interplanetary, and ground-based observations and provided further insight about Forbush decreases, *e.g.* their solar sources, interplanetary structures, important plasma/field parameters, and physical mechanisms playing an important role in deciding the amplitude and recovery characteristics of these decreases. However, regarding the relative importance of shock/sheath, ICME/MC (see, *e.g.*, Badruddin, Yadav, and Yadav, 1986; Cane, 1993; Babu *et al.*, 2013; Blanco *et al.*, 2013), one-step/two-step decrease (see, *e.g.* Cane, 2000, Jordan *et al.*, 2011), open/closed-field topology (Reames, Kahler, and Tylka, 2009; Richardson and Cane, 2011), and field turbulence/strength (Badruddin, Venkatesan, and Zhu, 1991; LeRoux and Potgieter, 1991; Wibberenz *et al.*, 1998; Dumbovic *et al.*, 2012), some questions still remain open.

It is important, therefore, to identify GCR-effective ICMEs and study their plasma/field properties, related features, and structures in relation to the Forbush decreases produced by them.

2. Data, Event-Selection, and Analysis

Using spacecraft data, useful catalogues of ICMEs have been prepared and published for various durations: *e.g.* 1996 – 2002 (Cane and Richardson, 2003), 1996 – 2000 (Gopalswamy *et al.*, 2001), 1995 – 2004 (Jian *et al.*, 2006), and 1996 – 2009 (Richardson and Cane, 2010). The catalogue by Richardson and Cane (2010) covers the whole of Solar Cycle 23 and gives a large amount of information and data as regards near-Earth ICME. The information as regards $\approx$300 ICMEs regarding their timing, associated structures/features, and some other related data formed the basis of this work. Furthermore, interplanetary plasma and field data were utilized from the NASA OMNIWEB data base. Neutron-monitor data for cosmic-ray intensity were used from two locations: Kiel and Calgary. Data for two neutron-monitor stations were utilized to confirm that the observed changes in intensity are real and not due to any instrumental problem or any local effect. These data are analyzed by the method of the superposed-epoch (Chree) analysis (Chree, 1912; Singh and Badruddin, 2006).

We utilize 14 years (1996 – 2009) of ICME data and study their response in GCR-intensity changes (decreases) as recorded by ground-based neutron monitors. For this statistical study of the GCR-response to these ICMEs, based on the degree of their "effectiveness" in producing depressions in GCR intensity, we have divided ICME "GCR-effectiveness" in five groups using Kiel data. In partial analogy with the so-called "geo-effectiveness", we name and divide the "GCR effectiveness" of ICMEs into five groups and call them, on the basis of their effects in modulating GCR intensity [I: counts per minute]: quiet ($\Delta I \approx 0.0$), small ($\Delta I \approx -0.01$ to -0.49 %); moderate ($\Delta I \approx -0.50$ to -1.49 %); large ($\Delta I \approx -1.50$ to -2.99 %); and very large (ΔI larger than -3.00 %) depressions. For calculating ΔI, the intensity data are first normalized to the 6 May 1997 value. Then the difference ΔI [%] is obtained from plots corresponding to each ICME event, *i.e.* the change in intensity ΔI [%] after the arrival of each ICME is found from these plots. We find that nearly half (48.4 %) of

the ICMEs either did not produce any depression in GCR intensity at all (17.3 %) or small depressions of less than 0.5 % (31.1 %). The rest of the ICMEs produce either the so-called moderate (27.3 %), large (11.8 %), and/or very large (12.5 %) intensity depressions. Such a wide range in GCR effectiveness of ICMEs motivated us to look for the distinctions, if any, in the properties of the average interplanetary plasma and field behavior during the passage of ICMEs responsible for the depressions of different ranges (small, moderate, large, and very large).

3. Results and Discussion

3.1. Average Plasma/Field Properties During Passage of ICMEs of Different GCR Effectiveness: Superposed Epoch Analysis

We have selected several interplanetary plasma/field parameters together with the GCR intensity as measured by two neutron monitors located at different positions on the Earth. The velocity of the solar wind and magnitude of the magnetic field are two important parameters for modulation of galactic cosmic rays. In addition to these two parameters, solar-wind velocity [V, km s^{-1}] and interplanetary magnetic-field vector [F, nT], we have selected, for our analysis, the standard deviation in the field vector [σ_{F}, nT] and the ratio σ_{F}/F as measures of fluctuations in magnetic-field vector. The plasma's β is also selected, as it provides information as regards the ratio of thermal [nkT] to magnetic [$B^2/2\mu_0$] pressures during the passage of ICME structures. The interplanetary electric field [E, mV m^{-1}] is also utilized as it is considered as an important modulation parameter. As a measure of GCR intensity at the Earth, we have utilized neutron-monitor data recorded at two stations: Calgary (latitude = 51.05 N, longitude = 114.08 W, cut-off rigidity $R_{\mathrm{c}} = 1.09$ GV) and Kiel (latitude = 54.30 N, longitude = 10.10 E, cut-off rigidity $R_{\mathrm{c}} = 2.36$ GV). The superposed-epoch analysis results with respect to arrival time (zero hour) of ICME disturbances of the five groups of ICMEs are shown in Figure 1a – 1e. These show the average amplitude and temporal profile of various parameters before the arrival, during, and after the passage of each group of ICMEs.

We observe that the GCR depression, in four out of five cases (see Figure 1a – 1e) starts [A] near zero hour [arrival time of ICME-related disturbance], a sharper decrease at first up to a few hours [B], a slower decrease until minimum intensity [C], and then recovery to pre-decrease level [D] taking a much longer time. These timings are shown by vertical lines [A, B, C, and D], respectively, in these figures. However, as shown in Figure 1a for the "quiet" group of ICMEs, there is essentially no decrease in GCR intensity after zero hour: *i.e.* arrival of the ICME. In this case, as evident from superposed results, the enhancements in V, F, and E as well as the level of σ_{F} are very small. Differences in amplitudes (Table 1) and time profiles (Figure 1a – 1e) can be seen.

The parameters V, F, and E increase sharply and reach a maximum level during the first few hours duration ($\approx$ six – ten hours) of the passage of the ICME structures. During this period, σ_{F} and σ_{F}/F are also were enhanced, indicating the dominance of the passage of the magnetically turbulent region. This period [AB] corresponds to a relatively faster rate of depression in GCR (see Figure 1a – 1e). During the period of subsequent slower decrease in GCR intensity up to lowest level [BC], although still high, the trend in V, F, and E is a decreasing one. Further, during this period, the values of σ_{F}, σ_{F}/F, and the plasma's β are very low, indicating the passage of a magnetically quiet but high-field region. This region [BC] probably corresponds to the passage of the CME/magnetic-cloud structure. Then the

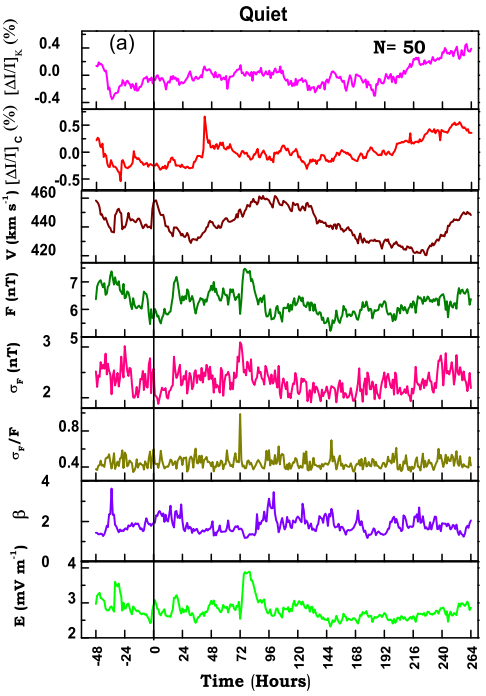

Figure 1 Superposed-epoch analysis of GCR intensity of neutron monitors at Kiel and Calgary and interplanetary-plasma field parameters; velocity [V], magnetic-field vector [F], standard deviation of field vector [σ_F], ratio [σ_F/F], plasma β, and electric field [E] with respect to arrival time (zero hour) of ICME disturbances producing depressions in GCR intensity of different range; (a) quiet, (b) small, (c) moderate, (d) large, and (e) very large depressions.

GCR recovery starts [C] and recovers during the period marked CD. During this period V, F, and E are decreasing but σ_F, σ_F/F, and β have almost stabilized to the pre-event level [before A].

It is known that the magnetic field is enhanced during the passage of shock/sheath regions (if and when developed ahead of CMEs) as well as in the following CME/magnetic-cloud structures (*e.g.* Klein and Burlaga, 1982; Badruddin, Yadav, and Yadav, 1986; Gosling, 1990; Venkatesan *et al.*, 1992; Badruddin and Singh, 2009). However, the field is likely to be turbulent inside the sheath region, while high-field ICME/magnetic-cloud structures are, in general, magnetically "quiet" (Zhang and Burlaga, 1988; Badruddin, Venkatesan, and Zhu, 1991; Liu *et al.*, 2006; Yu *et al.*, 2010). The initial step of fast decreasing intensity [AB] appears to coincide with the passage of a magnetically turbulent high-field region (*e.g.* shock/sheath); the next step of a slow decrease in intensity [BC] is likely to take place during the passage of the magnetically quiet high-field region (*e.g.* CME/magnetic cloud), and recovery is likely to start after the passage of this region and the recovery time [CD] may be influenced by the solar-wind speed profile. This is consistent with the hypothesis made by Badruddin, Venkatesan, and Zhu (1991) (see also Yu *et al.*, 2010). Another point to be mentioned here is that the last group, with maximum amplitude and duration of decrease, appears to be influenced by multiple ICME events passing one after the other. In Figure 1e, the substructures in plasma/field data, especially V and F, can be seen by multiple jumps after the start of the GCR intensity both during the decreasing and recovery phase. It is worth mentioning here that multiple ICMEs may also produce geomagnetic storms of larger intensity (see, *e.g.*, Farrugia and Berdichevsky, 2004; Gopalswamy, Yashiro, and Akiyama, 2007; Zhang *et al.*, 2007).

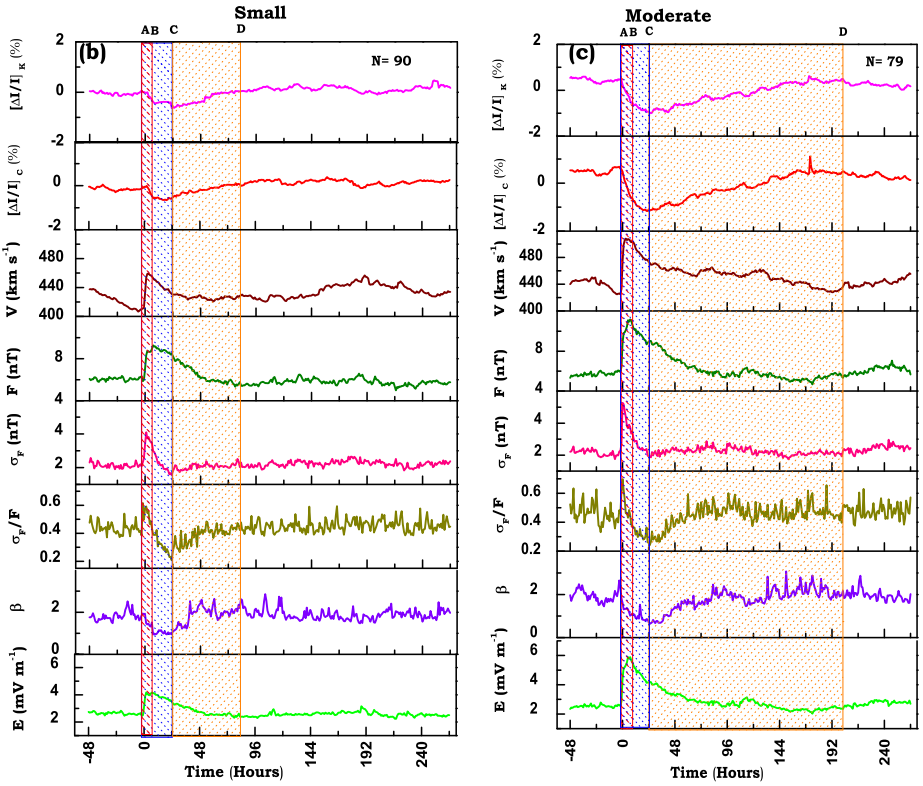

Figure 1 (*Continued*)

3.2. Distribution of Plasma/Field Parameters for ICMEs with Different GCR Effectiveness

Having studied the average plasma and field properties associated with ICMEs producing depressions of different range in GCR intensity, it will be useful to look for the differences in the distribution of some important plasma/field parameters (*e.g.* speed, magnetic, and electric fields) during the passage of ICMEs of different GCR effectiveness. These distributions for the peak values of speed [$\mathrm{km\,s^{-1}}$], vector magnetic field [nT], and electric field [$\mathrm{mV\,m^{-1}}$] producing different ranges (groups) of depressions in GCR intensity are shown, respectively, in Figures 2a, 2b, and 2c. To see the quantitative differences in different values and the spread in the distribution, the Gaussian $[y = y_0 + (A/w\sqrt{\pi}/2)\exp(-2(x - x_c)^2/w^2)]$ fitted curves are also shown over the respective histograms. From these plots we observe that, in general,

i) the frequency distribution shifts towards higher ranges of V_{max}, F_{max}, and E_{max} from the first group (quiet) towards the last group (very large) of ICMEs, producing GCR effectiveness of increasing range,
ii) the peak values of these parameters systematically shift towards higher values, and
iii) the spread in frequency distributions (full width at half maximum, $w_c = w\sqrt{\ln 4}$) is also larger for higher groups.

These values for different groups of GCR-effective ICMEs are tabulated in Appendix A (Tables 7, 8, and 9).

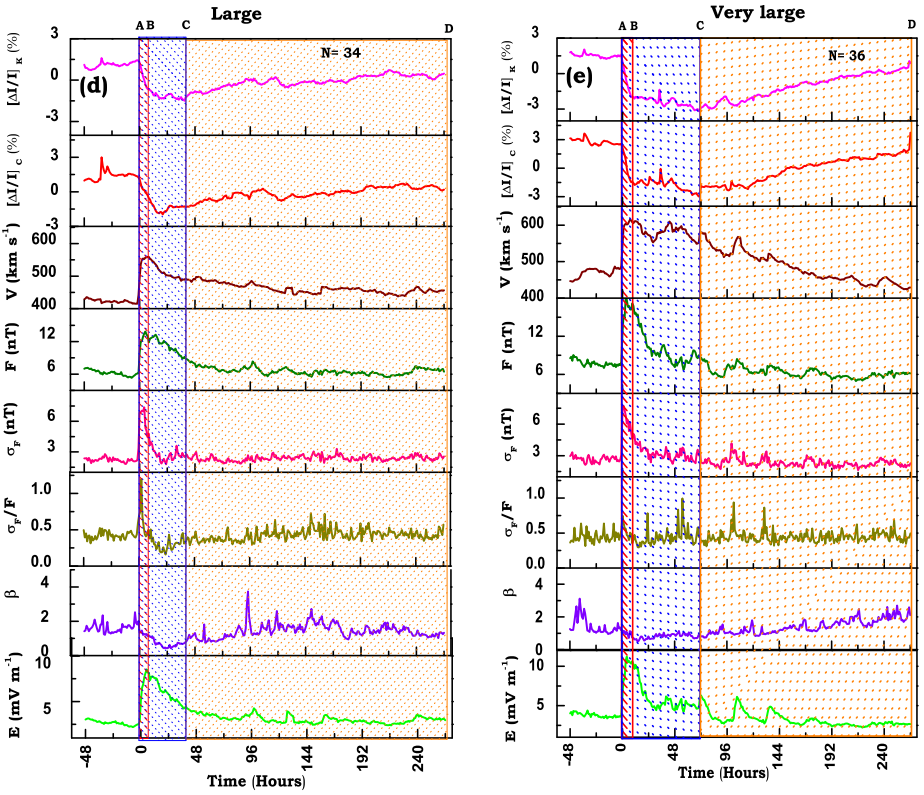

Figure 1 (*Continued*)

3.3. GCR Effectiveness of ICMEs Associated with Different Structures/Features: Superposed Epoch Analysis

We study the average plasma/field parameters and GCR effectiveness of ICMEs by dividing them into different groups based on their effectiveness in modulating GCR intensity, without consideration of any distinction in their types and/or associated features/structures. However, differences have been reported in plasma/field properties and the geomagnetic/ionosphere/cosmic-ray response of halo and non-halo CMEs (*e.g.* Gopalswamy, Yashiro, and Akiyama, 2007), magnetic-cloud/non-magnetic-cloud structure ICMEs (Marcz, 1992; Badruddin, 1998; Badruddin and Singh, 2009; Alves, Echer, and Ganzalez, 2011), ICMEs observed with bidirectional electron flows (BDEs) and without BDEs (Gosling *et al.*, 1987) and ICMEs driving a shock/sheath structures and those not associated with a shock/sheath region (*e.g.* Badruddin, 2002; Oh and Yi, 2012). Therefore, it is important to study in detail the relative GCR effectiveness of different structures/features associated/not associated with ICMEs. It will help us not only in identifying the structures/features of importance but also to understand the physical mechanisms playing important roles in the transient modulation of galactic cosmic rays.

We have performed a superposed-epoch analysis of GCR-intensity and interplanetary plasma/field parameters with respect to ICMEs associated with shocks (see Figure 3a) and those not associated with any shock (Figure 3b). It is observed that there is a large difference

Table 1 Averaged peak values and changes in various parameters due to ICMEs with different GCR effectiveness; quiet, small, moderate, large, and very large.

Group Name	ΔI (Kiel) [%]	ΔI (Cal) [%]	V_{max} [km s^{-1}]	ΔV [km s^{-1}]	F_{max} [nT]	ΔF [nT]	$\sigma_{F_{max}}$ [nT]	$\Delta\sigma_F$ [nT]	$(\sigma_F/F)_{max}$	$\Delta(\sigma_F/F)$	β_{max}	E_{max} [mV m^{-1}]	ΔE [mV m^{-1}]
Quiet [$\Delta I \approx 0.0$]	≈ 0.0	≈ 0.0	458	19	7.18	1.71	2.81	0.93	0.60	0.23	2.85	3.22	0.80
Small [$-0.01 \geq \Delta I \geq -0.49$]	-0.44	-0.58	460	52	9.25	3.22	4.09	1.96	0.62	0.24	2.52	4.21	1.80
Moderate [$-0.5 \geq \Delta I \geq -1.49$]	-1.44	-1.81	509	82	11.18	5.13	5.23	3.29	0.70	0.34	2.61	5.96	3.41
Large [$-1.5 \geq \Delta I \geq -2.99$]	-2.74	-3.37	559	143	13.73	8.27	7.17	5.02	1.18	0.78	2.46	8.47	6.11
Very large [$\Delta I \leq -3.0$]	-3.61	-4.13	612	150	18.10	10.82	7.93	5.39	0.74	0.31	1.53	11.25	7.67

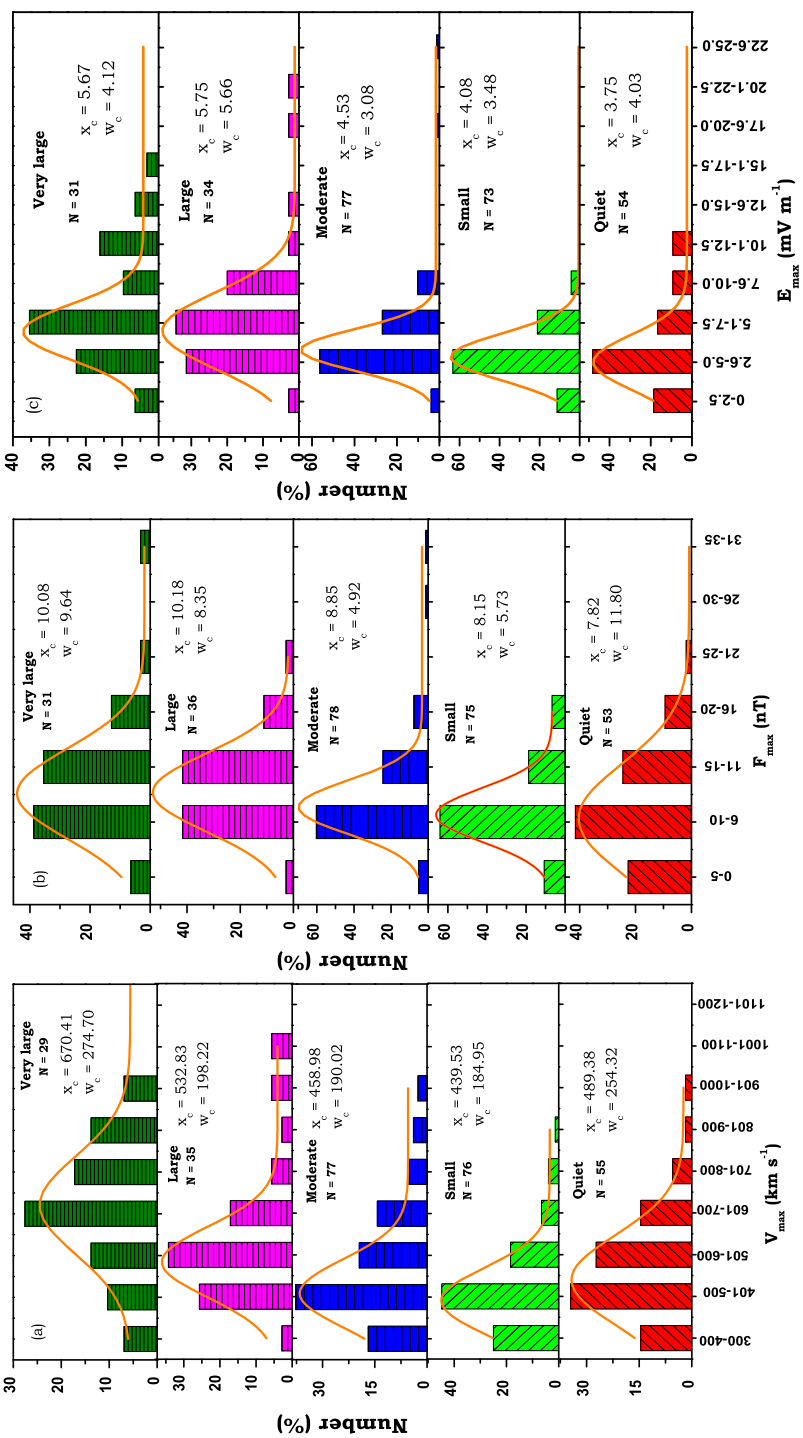

Figure 2 Frequency distribution and Gaussian-fitted curves for (a) V_{max} [km s^{-1}], (b) F_{max} [nT], and (c) E_{max} [mV m^{-1}], during the passage of ICMEs producing GCR-intensity depression of different range (quiet, small, moderate, large, and very large).

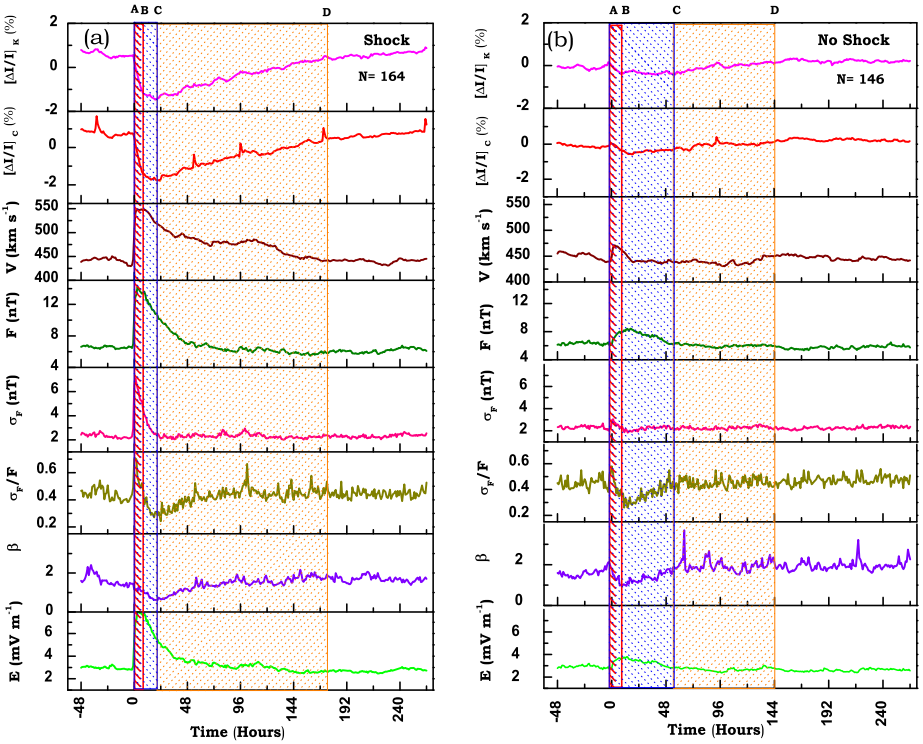

Figure 3 Superposed-epoch analysis results of GCR-intensity and interplanetary-plasma and field parameters; velocity [V], magnetic-field vector [F], standard deviation of field vector [σ_F], ratio [σ_F/F], plasma β, and electric field [E] with respect to passage of ICMEs associated with (a) a shock/sheath and (b) ICMEs not associated with a shock/sheath region.

between the amplitude and time profiles of GCR-intensity depressions in the two cases; the depression due to shock/sheath-associated ICMEs is a Forbush-decrease type with a much stronger decrease, while it is only a small depression in case of ICMEs without shocks. The average GCR effectiveness of shock-associated ICMEs is about four times higher than those not associated with shock/sheath regions (see Table 2a). The difference in enhancements of various parameters during the passage of shock-associated ICMEs and ICMEs without shocks can be seen in Figures 3a and 3b; enhancements in various parameters (V, F, σ_F, σ_F/F, and E) are larger during shock-associated ICMEs than ICMEs not associated with shocks. To quantify it, the ratio of the averaged peak values (*e.g.* V_{max}) and enhancements (*e.g.* ΔV) in various interplanetary plasma/field parameters during ICMEs with and without shock have also been calculated (see Table 2a). This ratio in peak values of various parameters [V_{max}, F_{max}, $\sigma_{F_{max}}$, and E_{max}] is about 1.2 to 2. However, the enhancements in individual parameters [ΔV, ΔF, $\Delta\sigma_F$, ΔE] are 3 to 6 times larger in case of shock-associated ICMEs than ICMEs without shocks.

Similar analyses have been performed by dividing the Solar Cycle 23 ICMEs in two groups:

i) those associated with bidirectional superthermal electron events (BDEs) and
ii) those not showing a BDE signature.

Table 2a Average GCR-intensity depression ΔI [%] at the Kiel and Calgary neutron monitors, peak values of interplanetary plasma/field parameters [V_{max}, F_{max}, $\sigma_{F_{max}}$, σ_F/F_{max}, β_{max}, and E_{max}], and enhancements in these parameters [ΔV, ΔF, $\Delta\sigma_F$, $\Delta(\sigma_F/F)$, and ΔE] due to ICMEs associated with/without shocks, BDEs, BDE-BIF, magnetic cloud, and halo structures. The calculated ratios of the values of different parameters due to ICME with/without particular structure are also given.

ICME Structure	ΔI [%] Kiel NM	ΔI [%] Calgary NM	V_{max} [km s^{-1}]	ΔV [km s^{-1}]	F_{max} [nT]	ΔF [nT]	$\sigma_{F_{max}}$ [nT]	$\Delta\sigma_F$ [nT]	$(\sigma_F/F)_{max}$	$\Delta(\sigma_F/F)$	β_{max}	E_{max} [mV m^{-1}]	ΔE [mV m^{-1}]
Shock	−1.92	−2.50	546	117	13.95	7.32	7.31	5.25	0.70	0.31	1.50	7.95	5.18
No Shock	−0.56	−0.62	471	31	8.42	2.33	2.97	0.89	0.59	0.32	2.04	3.78	1.08
Ratio	3.43	4.03	1.16	3.77	1.66	3.14	2.46	5.90	1.19	0.97	0.73	2.10	4.80
BDE	−1.63	−2.08	533	100	12.27	5.53	6.30	4.00	0.70	0.30	1.54	6.90	3.97
No BDE	−0.48	−0.61	472	42	8.55	2.95	3.33	1.46	0.58	0.22	2.27	3.98	1.56
Ratio	3.40	3.41	1.13	2.38	1.43	1.87	1.89	2.74	1.21	1.36	0.68	1.73	2.54
BDE-BIF	−2.12	−2.50	538	113	13.31	6.09	7.42	5.10	0.79	0.42	1.52	7.39	4.37
BDE-No BIF	−2.20	−3.40	562	119	15.68	9.91	7.97	6.01	1.13	0.72	1.77	10.04	7.36
Ratio	0.96	0.73	0.96	0.95	0.85	0.61	0.93	0.85	0.70	0.58	0.86	0.74	0.59
MC	−1.84	−2.50	512	98	13.96	7.82	6.40	4.40	0.84	0.63	2.49	7.67	5.14
No MC	−1.16	−1.24	526	86	10.39	3.85	4.85	2.60	0.68	0.27	1.45	5.59	2.75
Ratio	1.59	2.02	0.97	1.14	1.34	2.03	1.32	1.69	1.23	2.33	1.72	1.37	1.87
Halo	−2.31	−2.81	568	127	15.60	8.55	7.69	5.41	0.84	0.44	1.78	9.07	6.06
No Halo	−1.34	−1.84	535	87	11.03	4.44	5.19	2.94	0.68	0.35	1.76	6.03	3.11
Ratio	1.72	1.53	1.06	1.46	1.41	1.92	1.48	1.84	1.23	1.26	1.01	1.50	1.95

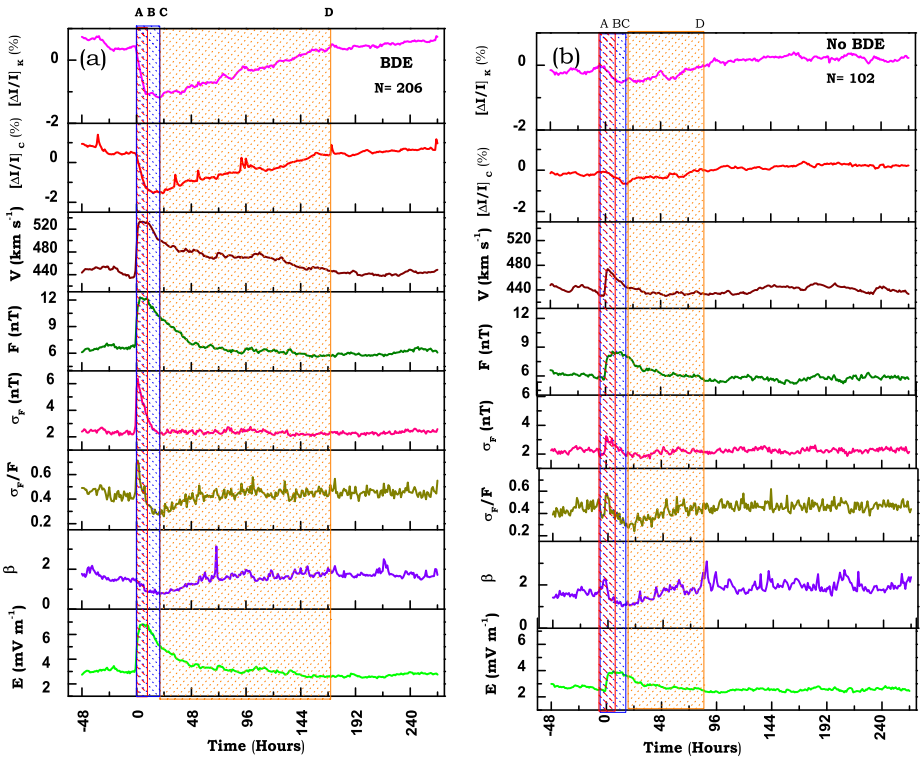

Figure 4 Superposed-epoch analysis results of GCR-intensity and interplanetary-plasma and field parameters: velocity [V], magnetic-field vector [F], standard deviation of field vector [σ_F], ratio [σ_F/F], plasma β, and electric field [E] due to ICMEs, (a) with bidirectional superthermal electron flows (BDEs), and (b) without BDEs.

The superposed-epoch plots of GCR-intensity and plasma/field parameters with respect to ICMEs with BDE and those not with BDE signature are shown in Figures 4a and 4b, respectively. Differences in amplitudes and time profiles in the GCR-intensity as well as interplanetary parameters are evident from these two figures. The GCR effectiveness of BDE-ICMEs as compared to non-BDE ICMEs is about 3.5 times larger, on the average (see Table 2a). The enhancements in peak values of various parameters (V_{max}, F_{max}, $\sigma_{F_{max}}$, E_{max}) are about 1.2 to 2 times higher in case of BDE-ICMEs than non-BDE ICMEs. However, the ratio of enhancements in various parameters (ΔV, ΔF, $\Delta\sigma_F$, ΔE) is about 2 to 3 times larger for BDE-ICMEs than non-BDE ICMEs; these values are tabulated in Table 2a. However, when BDE-ICMEs were divided on the basis of their occurrence with bidirectional energetic ion flows (BIF) and without BIF signatures, and superposed-epoch analysis of GCR-intensity and solar-wind parameters were performed with respect to arrival of BDE-ICME with and without BIFs, no great difference in their GCR effectivenesses was found except some difference in temporal profiles (see Figures 5a, 5b, and Table 2a). Similarly the changes in solar plasma and field parameters, considered here, are not very different in the two cases.

We have considered two sets of Solar Cycle 23 ICMEs:

i) those reported as magnetic clouds and
ii) those whose plasma and field properties are not similar to those of magnetic clouds.

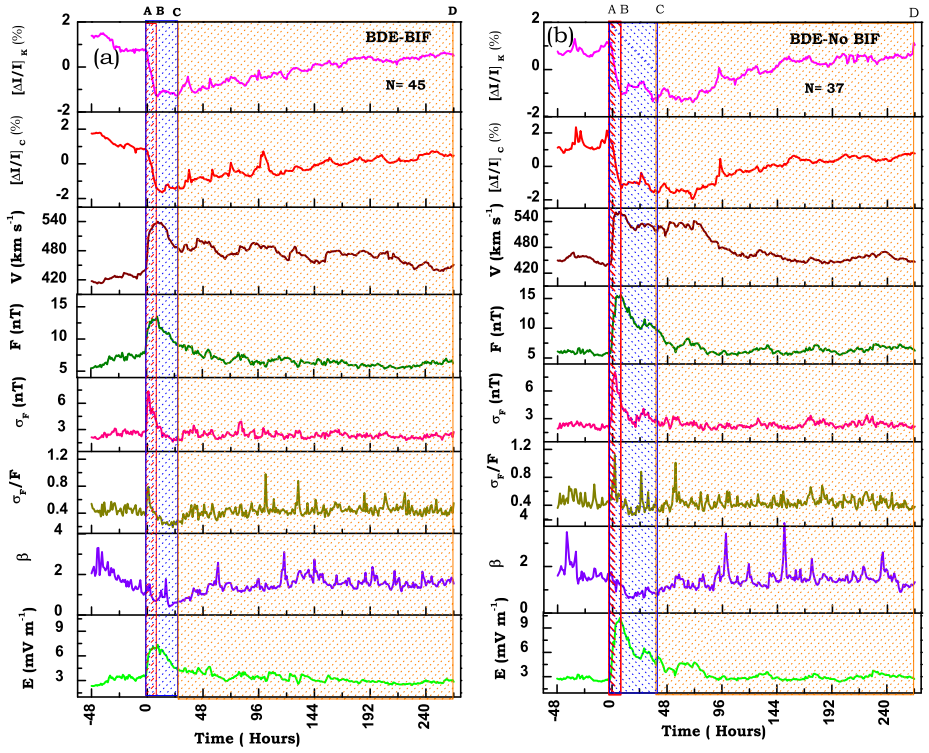

Figure 5 Superposed-epoch analysis results of GCR-intensity and interplanetary-plasma and field parameters; velocity $[V]$, magnetic-field vector $[F]$, standard deviation of field vector $[\sigma_F]$, ratio $[\sigma_F/F]$, plasma β, and electric field $[E]$ with respect to (a) ICMEs with bidirectional superthermal electron flows (BDEs) as well as bidirectional energetic ion flows (BIFs), and (b) ICMEs with BDEs but without BIFs.

To see whether magnetic clouds are more GCR effective than non-magnetic cloud ICMEs or not, we have adopted a similar approach as to that used in earlier cases, and we performed superposed-epoch analysis of GCR-intensity and plasma/field parameters with reference to

i) ICMEs with magnetic cloud structures and
ii) ICMEs not showing magnetic cloud features.

It is found (see Figures 6a and 6b) that magnetic clouds are, on average, about twice as GCR-effective as non-magnetic cloud ICMEs. As regards the differences in variations in plasma/field parameters, it is observed that, although the average speed and enhancement in it is almost same in two cases, the vector magnetic-field and electric-field enhancement in the case of magnetic clouds is almost twice as large as in the case of non-magnetic cloud ICMEs (see Table 2a).

A superposed-epoch analysis with respect to ICMEs related to halo CMEs and non-halo CMEs also shows a difference in the GCR effectiveness of two type of CMEs; halo CMEs are more GCR-effective than non-halo CMEs; the relative GCR-effectiveness is about 1.5 times larger for halo CME as than non-halo CMEs. Differences in solar-wind speed, IMF strength, and electric fields are also observed (see Figures 7a, 7b, and Table 2a).

From the above discussions it is clear that the ICMEs associated with shocks/BDEs/MCs/halo-CMEs are more GCR-effective than ICMEs not associated with these structures/features.

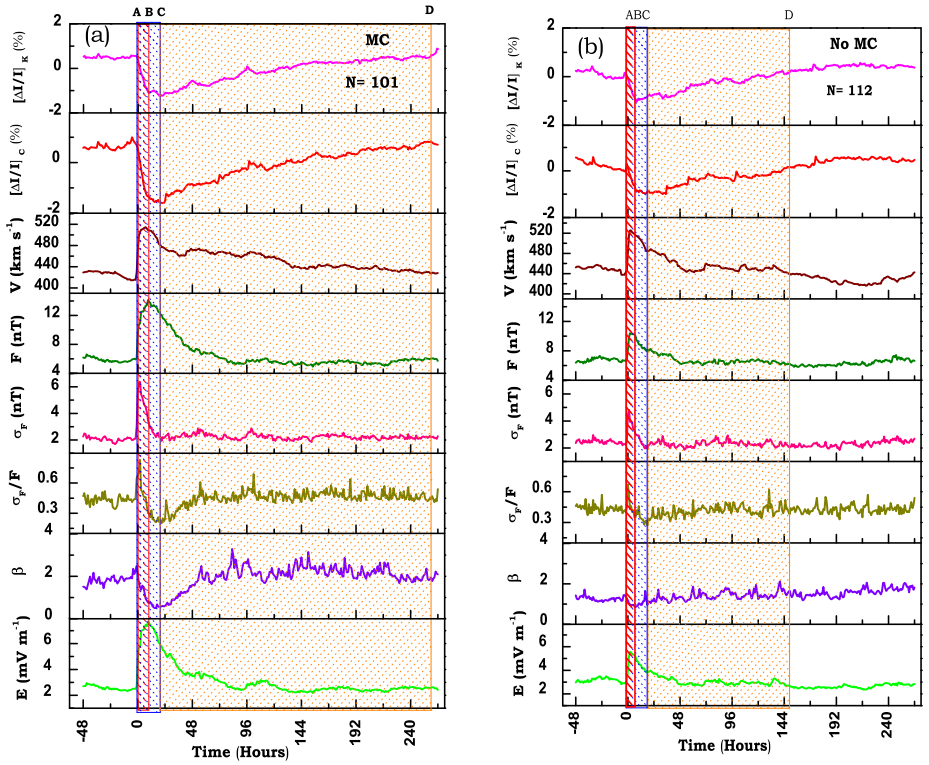

Figure 6 Superposed-epoch analysis results of GCR-intensity and interplanetary-plasma and field parameters; velocity [V], magnetic-field vector [F], standard deviation of field vector [σ_F], ratio [σ_F/F], plasma β, and electric field [E] with respect to (a) ICMEs reported to be magnetic clouds (MC) and (b) ICMEs not showing magnetic-cloud structure (non-MC).

Each group (BDE/MC/halo) was subdivided into shock/no shock cases. A large difference in their GCR-effectiveness is observed; shock/sheath-associated BDE/MC/halo ICMEs are much more GCR-effective than those not associated with any shock/sheath region (see Table 2b). This result again emphasizes the role of magnetic turbulence in sheath regions as is evident from the ratios of $\Delta\sigma_F$ (see also Badruddin, Venkatesan, and Zhu, 1991; Yu *et al.*, 2010; Dumbovic *et al.*, 2011).

We have shown that the GCR effectiveness of ICMEs associated/not associated with different structures/features is not similar, and there are distinctions in the distribution of different ranges of GCR depressions from quiet, small, moderate, large, up to very large depressions. Therefore, it is important to look for the distribution of various plasma/field parameters. We have studied these distributions for three parameters [V_{max}, F_{max}, and E_{max}] by dividing these parameters into suitable bins. These distributions for V_{max} are shown for shock/non-shock ICMEs, BDE/non-BDE ICMEs, magnetic cloud/non-magnetic cloud ICMEs, and halo/non-halo ICMEs (Figure 10 in Appendix B). Similar distributions for F_{max} (Figure 11 in Appendix B) and E_{max} (Figure 12 in Appendix B) are also plotted. Central peak values [x_c], full width at half maximum [w_c], and the product $x_c w_c$ are also calculated for each structure and the parameters after fitting a Gaussian function. These values are tabulated in Appendix C (Tables 10, 11, and 12). A clear difference in the values of the frequency distributions [x_c, w_c, and $x_c w_c$] for different parameters [V_{max}, F_{max}, and E_{max}] due

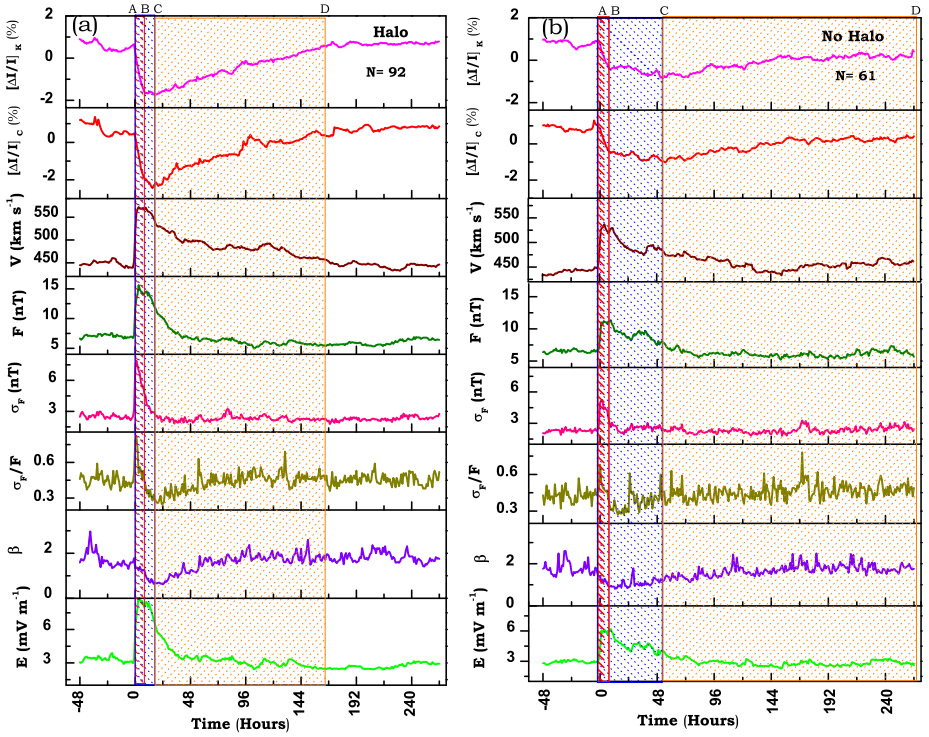

Figure 7 Superposed-epoch analysis results of GCR-intensity and interplanetary-plasma and field parameters: velocity $[V]$, magnetic-field vector $[F]$, standard deviation of field vector $[\sigma_F]$, ratio $[\sigma_F/F]$, plasma β, and electric field $[E]$ for ICME structures due to (a) halo CMEs and (b) for ICME structures other than halo CMEs (non-halo).

to shock/no-shock, BDE/non-BDE, magnetic cloud/non-magnetic cloud and halo/non-halo ICMEs can be seen (see Appendix B and Appendix C).

3.4. GCR Effectiveness of ICMEs with Different Structures/Features: Statistical Results

As discussed in Section 3.1, we have divided the GCR effectiveness of ICMEs into five convenient groups, on the basis of their effects in modulating GCR intensity:

i) quiet ($\Delta I \approx 0.0$);
ii) small ($\Delta I \approx -0.01$ to -0.49 %);
iii) moderate ($\Delta I \approx -0.50$ to -1.49 %);
iv) large ($\Delta I \approx -1.50$ to -2.99 %), and
v) very large (ΔI larger than -3.00 %) depressions.

The contributions of ICMEs associated/not associated with different structures/features to the different groups of depressions (quiet, small, moderate, large, and very large) are given for shock/no-shock ICMEs, BDE/No-BDE ICMEs, BDE-BIF/BDE-no-BIF, magnetic cloud/non-magnetic cloud, and halo/non-halo ICMEs (see Table 3). It can be seen from this table that, in general, shock/BDE/MC/halo ICMEs are more often associated with "large" and "very large" GCR effectiveness than the no-shock/no-BDE/no-MC/no-halo ICMEs. This difference is most prominent in the case of shock/sheath-associated

Table 2b Average GCR-intensity depression (%) at the Kiel and Calgary neutron monitors, peak values of interplanetary plasma-field parameters [V_{max}, F_{max}, $\sigma_{F_{max}}$, $(\sigma_F/F)_{max}$, β_{max} and E_{max}] and enhancements in these parameters [ΔV, ΔF, $\Delta\sigma_F$, $\Delta(\sigma_F/F)$, and ΔE] due to BDE ICMEs associated with/without shock, magnetic clouds with/without shock, halo CMEs with/without shock structures. The calculated ratios of different parameters due to ICME of different features with/without shock are also given.

ICME Structure	ΔI [%] Kiel NM	ΔI [%] Calgary NM	V_{max} [km s^{-1}]	ΔV [km s^{-1}]	F_{max} [nT]	ΔF [nT]	$\sigma_{F_{max}}$ [nT]	$\Delta\sigma_F$ [nT]	$(\sigma_F/F)_{max}$	$\Delta(\sigma_F/F)$	β_{max}	E_{max} [mV m^{-1}]	ΔE [mV m^{-1}]
BDE with shock	−2.28	−2.82	556	132	14.93	8.18	7.56	5.44	0.76	0.36	1.37	8.39	5.46
BDE without shock	−0.87	−1.26	501	51	9.52	2.96	4.48	2.26	0.76	0.35	1.78	5.17	2.18
Ratio	2.62	2.23	1.11	2.59	1.57	2.76	1.69	2.41	1.00	1.03	0.77	1.62	2.50
MC with shock	−2.69	−3.59	555	134	16.20	10.07	8.06	5.92	1.01	0.45	1.91	8.85	6.24
MC without shock	−0.60	−0.83	441	44	11.23	6.22	3.27	1.55	0.81	0.43	6.45	3.68	1.65
Ratio	4.48	4.32	1.26	3.04	1.44	1.62	2.46	3.82	1.25	1.05	0.30	2.40	3.78
Halo with shock	−3.02	−3.61	585	156	17.30	11.01	9.07	6.81	0.85	0.42	1.43	10.08	7.38
Halo without shock	−1.27	−1.41	551	90	11.45	4.06	5.23	2.93	0.84	0.51	2.78	6.62	3.06
Ratio	2.38	2.56	1.06	1.73	1.51	2.71	1.73	2.32	1.01	0.82	0.51	1.52	2.41

Table 3 Comparative distribution of relative GCR effectiveness (quiet, small, moderate, large, and very large) due to ICMEs associated/not associated with different structures.

Number [%]					
ICME Structure	Quiet $\Delta I \approx 0.0$	Small $-0.01 \geq \Delta I \geq -0.49$ [%]	Moderate $-0.50 \geq \Delta I \geq -1.49$ [%]	Large $-1.50 \geq \Delta I \geq -2.99$ [%]	Very large $\Delta I \leq -3.00$ [%]
Shock	14.8	18.3	29.6	19.7	17.6
No Shock	22.2	37.3	28.6	6.3	5.6
BDE	14.8	24.8	30.2	14.8	15.4
No BDE	25.9	25.9	32.9	11.8	3.5
MC	14.0	21.5	35.5	14.0	15.0
No MC	20.2	28.1	23.6	15.7	12.4
Halo	24.7	14.8	23.5	21.0	16.0
No Halo	10.4	20.8	37.5	12.5	18.8

Table 4 Correlation coefficient [R] and slope from the best-fit linear curve between average GCR-intensity change and various parameters obtained from superposed-epoch analysis during the passage of ICMEs with different GCR effectiveness and associated/not associated with different structures/features.

Serial No.	Parameters	ΔI [%]	
		Linear fit	
		R	Slope
1	V_{max} [km s^{-1}]	−0.91	-0.02 ± 0.00
2	ΔV [km s^{-1}]	−0.95	-0.02 ± 0.00
3	F_{max} [n T]	−0.96	-0.37 ± 0.03
4	ΔF [n T]	−0.94	-0.37 ± 0.03
5	$\sigma_{F_{max}}$ [n T]	−0.95	-0.57 ± 0.04
6	$\Delta\sigma_F$ [n T]	−0.95	-0.60 ± 0.05
7	$(\sigma_F/F)_{max}$	−0.65	-4.52 ± 1.27
8	$\Delta(\sigma_F/F)$	−0.50	-3.92 ± 1.65
9	E_{max} [mV m^{-1}]	−0.97	-0.48 ± 0.03
10	ΔE [mV m^{-1}]	−0.98	-0.52 ± 0.02
11	β_{max}	0.41	0.42 ± 0.22

ICMEs rather than those not associated with the shock/sheath region. This again emphasizes the role of the shock/sheath region in producing larger depressions in GCR intensity (see also Zhang and Burlaga, 1988; Badruddin, Venkatesan, and Zhu, 1991; Lockwood, Webber, and Debrunner, 1991; Oh, Yi, and Kim, 2008; Yu *et al.*, 2010; Dumbovic *et al.*, 2012).

3.5. Decrease Amplitude and Its Dependence on Interplanetary Parameters: Quantitative Relationship

In Tables 1 and 2a, 2b, we have tabulated the amplitudes/enhancements in various parameters including GCR intensity obtained from superposed plots. Using the values given in these tables, we obtained the linear relationship between the GCR-intensity depression ΔI [%] at Kiel and other tabulated parameters. The linear-correlation coefficients so obtained and the rate of change of GCR intensity with various parameters are given in Table 4. Scatter plots and best-fit linear curves with magnetic and electric fields are also plotted in Figures 8a and b. However, it should be noted that the linear fit is obtained from the averages, which are not independent, as the same events are present in various classes of data points. On the basis of these fits, using averaged values of parameters, the GCR intensity is found to decrease at a rate of −0.37 % per unit increase in the vector magnetic field [nT] and −0.48 % per unit increase in the electric field [mV m^{-1}] during the passage of ICMEs.

3.6. Recovery Characteristics of Depressions in GCR-Intensity Due to ICMEs

We have studied the recovery characteristics of GCR-intensity depression for the averaged recovery profiles obtained due to depressions of different GCR effectiveness (small, moderate, large, and very large depressions) and due to ICMEs with different features/structures (shock/no-shock, BDE/no-BDE, magnetic cloud/non-magnetic cloud, halo/non-halo ICMEs). We have also fitted an exponential [$y = y_0 + Ae^{(-x/\tau)}$] to these recovery profiles (see Figures 13, 14, and 15 in Appendix D and Table 5). The characteristic recovery time [τ] increases with GCR effectiveness (Table 5); it is larger for the shock-associated ICMEs than for those not associated with shocks. A similar trend in differences in characteristic time can be seen in the case of BDE/non-BDE ICME, and halo/non-halo

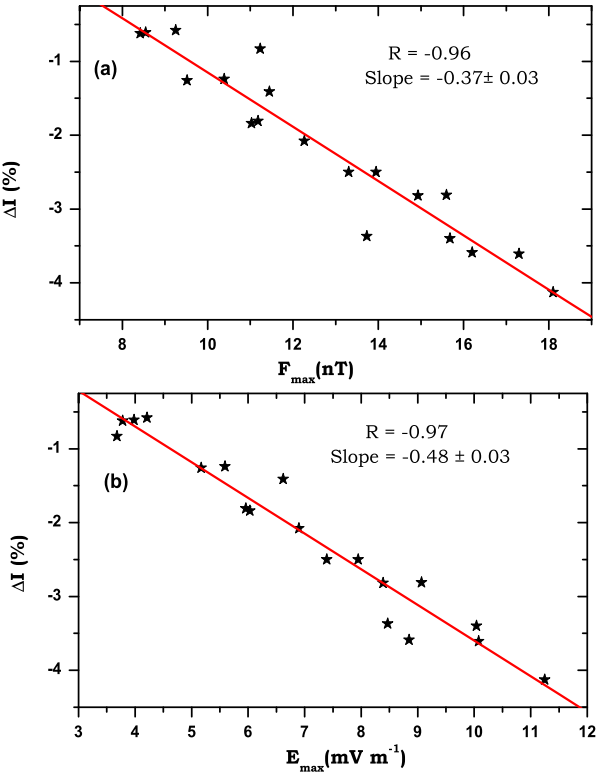

Figure 8 Best-fit linear curve between averaged GCR-intensity depression [ΔI, %] and (a) magnetic-field amplitude [$F_{\max}$, nT], (b) electric-field amplitude [$E_{\max}$, mV m^{-1}] due to ICMEs with different GCR-effectiveness and ICMEs associated/not associated with different structures/features.

ICMEs. The characteristic recovery time [τ] is larger for BDE-ICMEs than for non-BDE-ICMEs and it is larger for halo ICMEs than for non-halo ICMEs (Table 5).

We have also tried to search for the parameter out of those considered here [V, F, σ_{F}, σ_{F}/F, β, and E] that best correlates with the rate of change in the intensity of GCR during its recovery. Out of these parameters, we find that, during recovery, it is better correlated with solar-wind speed (even better than F and E), at least during recovery after passage of shock/sheath-associated ICMEs, BDE-associated ICMEs and halo-CMEs (see Table 6).

From our averaged plots, we have also attempted to find whether the speed of the ICME disturbance during its passage to Earth is related to the recovery time (*i.e.* the time period from the minimum of the depression to the point of GCR intensity returning to the pre-decrease value) of the GCR-intensity depression or not. A linear-regression plot (Figure 9) between $V_{\max}$ and the recovery time of the depression shows that the speed of the ICME-related disturbance may influence the recovery time after the depression.

4. Summary and Conclusions

From the statistical and superposed-epoch analysis presented in this article, we summarize our conclusions:

- Nearly half (48.4 %) of the ICMEs identified in the near-Earth interplanetary plasma/field data near the Earth either do not produce any depression in GCR intensity (17.3 %) or produce small depressions of less than 0.5 % (31.1 %). The rest of the ICMEs either produce

Table 5 Characteristic recovery time [τ, hours] of GCR intensity with determination coefficient [R^2] due to ICMEs of different GCR-effectiveness, ICMEs associated/not associated with different structures/features and different ICMEs with/without shocks.

GROUP/ICME Structure	Recovery Phase	
	Exponential fit	
	R^2	τ [hours]
Small	0.79	30.83 ± 2.16
Moderate	0.89	71.24 ± 4.64
Large	0.78	100.80 ± 13.78
Very large	0.97	333.33 ± 55.34
Shock	0.99	146.75 ± 5.11
No Shock	0.89	57.41 ± 3.57
BDE	0.98	158.42 ± 7.28
No BDE	0.87	61.78 ± 3.89
MC	0.97	118.48 ± 5.16
No MC	0.96	122.46 ± 6.38
Halo	0.98	109.26 ± 3.78
No Halo	0.91	75.16 ± 5.56
BDE with Shock	0.98	173.13 ± 7.63
BDE without Shock	0.91	163.28 ± 16.46
MC with Shock	0.98	144.71 ± 6.92
MC without Shock	0.52	36.40 ± 5.18
Halo with Shock	0.98	112.18 ± 3.70
Halo without Shock	0.86	58.36 ± 4.24

Table 6 Correlation coefficients between the rate of change in the GCR intensity during the recovery phase and various parameters for ICMEs associated with different structures and different GCR effectiveness.

ICME Structure	Recovery Phase					
	Correlation [R] between ΔI and different parameters during recovery					
	V	F	σ_F	σ_F/F	β	E
Shock	−0.94	−0.80	−0.13	0.58	0.82	−0.87
No- Shock	−0.18	−0.65	0.28	0.50	0.45	−0.67
BDE	−0.93	−0.82	−0.37	0.60	0.70	−0.87
No-BDE	−0.47	−0.67	0.51	0.03	0.64	−0.66
MC	−0.92	−0.75	−0.24	0.54	0.58	−0.84
No-MC	−0.75	−0.72	0.07	0.47	0.56	−0.67
Halo	−0.92	−0.78	−0.01	0.61	0.77	−0.82
No-Halo	−0.59	−0.32	0.25	0.33	0.59	−0.53
Small	−0.33	−0.92	0.52	0.72	0.58	−0.91
Moderate	−0.82	−0.87	−0.32	0.51	0.76	−0.89
Large	−0.72	−0.73	0.02	0.38	0.45	−0.69
Very large	−0.95	−0.64	−0.36	−0.05	0.75	−0.67

the so-called moderate (27.3 %), large (11.8 %), or very large (12.5 %) depressions in GCR intensity.

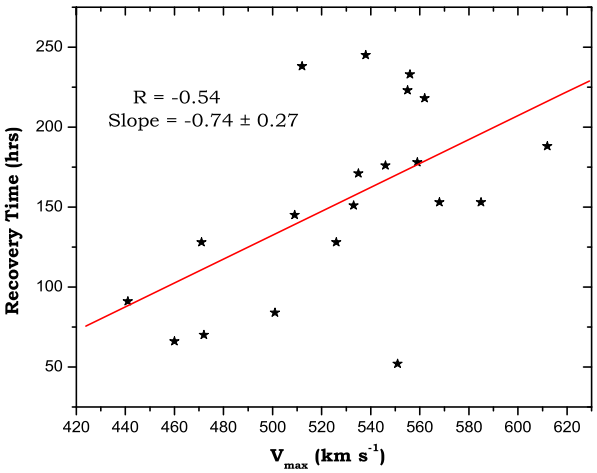

Figure 9 Linear-regression plot between V_{max} [km s^{-1}] and GCR-intensity recovery time [hours], obtained from superposed-epoch plots, due to ICMEs with different GCR effectiveness and ICMEs associated/not associated with different structures/features.

- The average GCR-intensity depression profile due to the four groups of GCR effective ICMEs (small, moderate, large, and very large) with successively increasing depressions start at the arrival of ICME-related disturbance, with a relatively sharper decrease at first up to a few hours, followed by a slower decrease until minimum intensity is reached. Subsequently recovery starts, reaching the pre-decrease level in a much longer time (a few days).
- It is found from the frequency distribution of plasma/field parameter (speed, magnetic-field vector, and electric fields) that the distribution of these parameters, their peak values, and the spread of frequency distribution shift successively towards the higher side from the quiet, small, moderate, large, to very large group of GCR effective ICMEs.
- Based on the superposed-epoch analysis, we found that the GCR effectiveness of shock-associated ICMEs, on average, is about 4 times larger than that of those not associated with a shock/sheath region. Similar analyses also reveal that the ICMEs with bidirectional superthermal electron (BDE) signatures are about 3.5 times more geo-effective than ICMEs not associated with BDEs. Further, ICMEs with a magnetic-cloud structure are about twice as GCR effective as ICMEs observed to have non-magnetic-cloud structures. The ICMEs due to halo-CMEs are found to be about 1.5 times more GCR-effective than those due to non-halo CMEs. Enhancements in various plasma and field parameters are also found to be larger due to ICMEs associated with shocks/BDEs/MCs/halo-CMEs than those not associated with these structures/features.
- From statistical analysis of five groups of GCR-effective ICMEs (quiet, small, moderate, large, and very large) associated/not associated with different structures/features, we found that "large" and "very large" depressions together are much larger (37.3 %) due to shock-associated ICMEs than those not associated with shocks (11.9 %). Similarly a larger number of large and very large depressions in GCR intensity are associated with ICMEs with BDE rather than to non-BDE ICMEs, magnetic clouds rather than to ICMEs having another than the magnetic-cloud structure, and ICMEs due to halo ICMEs rather than due to non-halo ICMEs.
- The central peak values, full width at half maximum, and their products obtained from Gaussian fits to distributions of different parameters [V_{max}, F_{max}, and E_{max}] due to shock, BDE, MC, and halo ICMEs are larger than those not associated with these structures/features.

- From the best-fit linear relation between averaged GCR-intensity depressions [%] and maximum values of magnetic [$F_{\max}$] and electric fields [$E_{\max}$], we found that GCR intensity decreases at the rate of ≈ 0.40 % per unit increase in vector magnetic field [nT] and ≈ 0.50 % per unit increase in electric field [mV m^{-1}].
- An exponential fit to the recovery of GCR intensity reveals that the characteristic recovery time is much larger for shock/BDE/MC/halo-CME-associated ICMEs than those not associated with these structures/features.
- During recovery, the temporal variation of the GCR intensity is found to be better correlated with simultaneous variation in solar-wind speed than other parameters [*e.g.* F and E].
- The speed of ICME-related disturbances appears to be influential in deciding the total recovery time of the depressions.

Acknowledgements Useful catalogs of ICMEs/CMEs/magnetic clouds prepared and published/displayed on websites (especially by I.G. Richardson and H.V. Cane, N. Gopalswamy and R.P. Lepping) are highly appreciated. We acknowledge the use of solar and plasma/field data through NASA/GSFC OMNI Web interface. K. Röhrs and R.B. Hicks, PIs of the Kiel and Calgary neutron monitors, respectively, are also thanked for making the data available in usable format. Use of these data is acknowledged with gratitude. We also thank the reviewer for constructive and helpful comments.

Appendix A

Table 7 Gaussian-fit parameters for the distribution of maximum solar-wind velocity [$V_{\max}$], central-peak value of $V_{\max}$ [x_c], width [w], full width at half maximum [w_c], and the product $x_c w_c$ during the passage of ICMEs of different GCR effectiveness.

Group	Gaussian-fit parameters for $V_{\max}$				
	R^2	x_c	w	w_c	$x_c w_c$ [10^4]
Small	0.99	439.53± 4.99	157.08± 10.59	184.95	8.13
Moderate	0.93	458.98± 14.96	161.39± 31.42	190.02	8.72
Large	0.97	532.83± 8.51	168.35± 19.20	198.22	10.56
Very large	0.89	670.41± 20.30	233.31± 56.43	274.70	18.42

Table 8 Gaussian-fit parameters for the distribution of maximum magnetic field [$F_{\max}$], central-peak value of $F_{\max}$ [x_c], width [w], full width at half maximum [w_c], and the product $x_c w_c$ during the passage of ICMEs of different GCR effectiveness.

Group	Gaussian-fit parameters for $F_{\max}$				
	R^2	x_c	w	w_c	$x_c w_c$
Small	0.99	8.15 ± 0.0	4.87 ± 0.00004	5.73	46.70
Moderate	0.99	8.85 ± 0.55	4.81 ± 1.18	5.66	50.09
Large	0.98	10.18 ± 0.46	7.09 ± 2.12	8.35	85.00
Very large	0.98	10.08 ± 0.36	8.19 ± 0.99	9.64	97.17

Table 9 Gaussian-fit parameters for the distribution of maximum electric field [E_{max}], central-peak value of E_{max} [x_c], width [w], full width at half maximum [w_c], and the product $x_c w_c$ during the passage of ICMEs of different GCR effectiveness.

Group	Gaussian-fit parameters for E_{max}				
	R^2	x_c	w	w_c	$x_c w_c$
Small	0.99	4.08 ± 0.06	2.96 ± 0.09	3.49	14.24
Moderate	0.97	4.53 ± 0.20	2.62 ± 0.47	3.08	13.95
Large	0.96	5.75 ± 0.23	4.81 ± 0.52	5.66	32.54
Very large	0.84	5.67 ± 0.40	3.50 ± 0.89	4.12	23.36

Appendix B

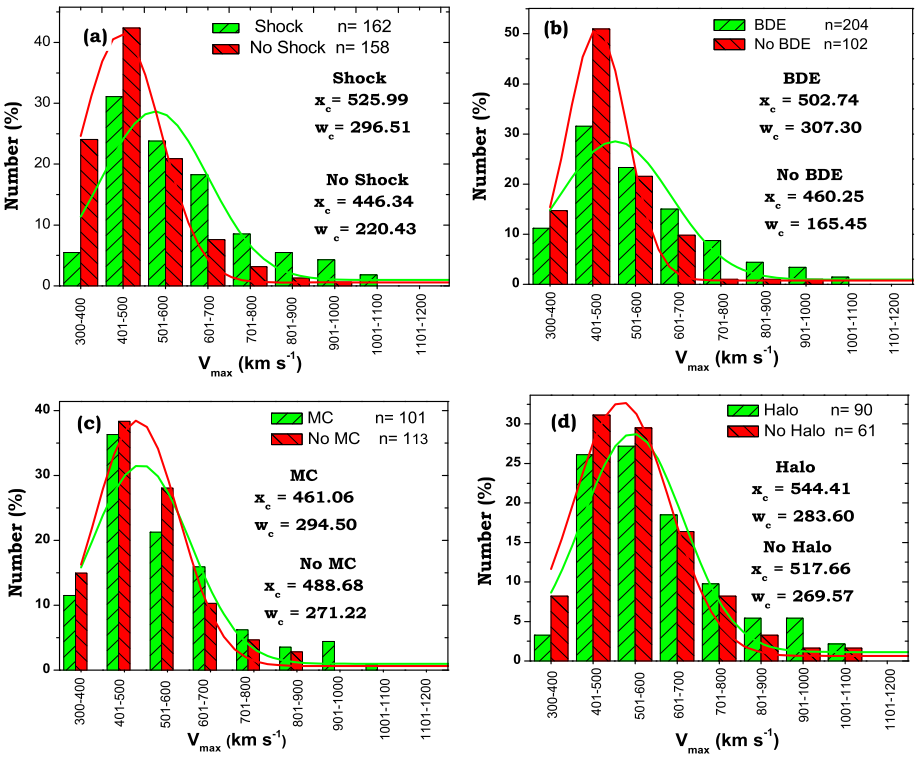

Figure 10 Frequency distribution of maximum speed, [V_{max}, $\mathrm{km\,s^{-1}}$] observed during the passage of ICMEs associated/not associated with (a) shocks, (b) BDEs, (c) magnetic clouds, and (d) halo CMEs. Gaussian best-fit curves representing the distribution of ICMEs are also shown in the figure. The central-peak values [x_c] and full widths at half maximum [w_c] obtained from the fits.

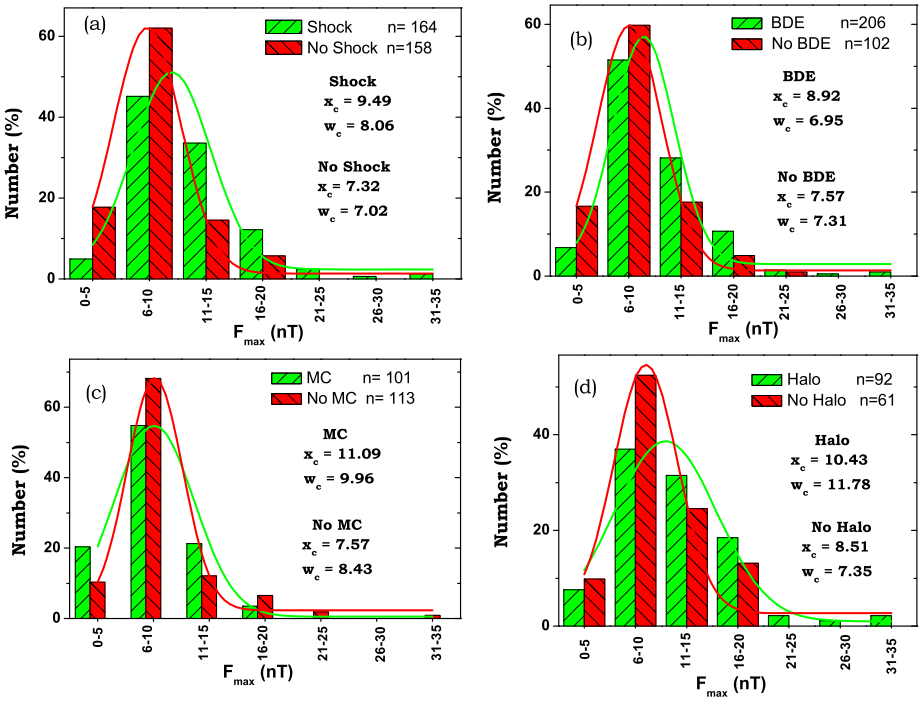

Figure 11 Frequency distribution of maximum magnetic-field vector [$F_{\max}$, nT] observed during the passage of ICMEs associated/not associated with (a) shocks, (b) BDEs, (c) magnetic clouds, and (d) halo CMEs. Gaussian best-fit curves representing the distribution of ICMEs are also shown in the figure. The central peak values [x_c] and full widths at half maximum [w_c] obtained from the fits.

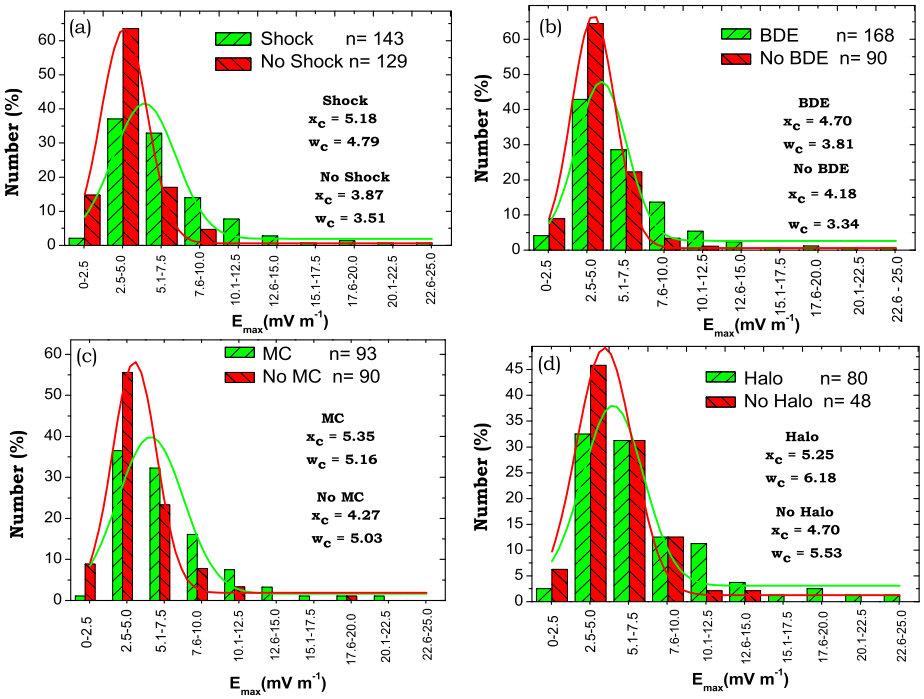

Figure 12 Frequency distribution of maximum electric field, [$E_{\max}$, mV m^{-1}] observed during the passage of ICMEs associated/not associated with (a) shocks, (b) BDEs, (c) magnetic clouds, and (d) halo CMEs. Gaussian best-fit curves representing the distribution of ICMEs are also shown in the figure. The central-peak values [x_c] and full widths at half maximum [w_c] obtained from the fits.

Appendix C

Table 10 Gaussian-fit parameters for the distribution of maximum solar-wind velocity [$V_{\max}$], central-peak value of $V_{\max}$ [x_c], width [w], full width at half maximum [w_c], and the product $x_c w_c$ during the passage of ICMEs with different structures/features.

ICME Structure	Gaussian-fit parameters for $E_{\max}$				
	R^2	x_c	w	w_c	$x_c w_c$ [10^4]
Shock	0.90	526.00 ± 14.84	251.83 ± 33.31	296.51	15.60
No Shock	0.99	446.34 ± 3.72	187.22 ± 8.23	220.43	09.84
BDE	0.94	502.74 ± 12.13	261.00 ± 28.17	307.30	15.45
No BDE	0.98	460.25 ± 4.52	140.52 ± 7.67	165.45	07.61
MC	0.93	461.06 ± 14.18	250.12 ± 33.72	294.50	13.58
No MC	0.91	488.68 ± 13.42	230.35 ± 30.58	271.22	13.25
Halo	0.93	544.41 ± 12.05	240.86 ± 26.52	283.60	15.44
No Halo	0.97	517.66 ± 7.37	228.95 ± 16.29	269.57	13.95

Table 11 Gaussian-fit parameters for the distribution of maximum magnetic field [$F_{\max}$], central-peak value of $F_{\max}$ [x_c], width [w], full width at half maximum [w_c], and the product $x_c w_c$ during the passage of ICMEs with different structures/features.

ICME Structure	Gaussian-fit parameters for $F_{\max}$				
	R^2	x_c	w	w_c	$x_c w_c$
Shock	0.96	9.49 ± 0.42	6.85 ± 1.39	8.06	76.49
No Shock	0.99	7.32 ± 0.23	5.96 ± 0.34	7.02	51.40
BDE	0.97	8.92 ± 0.44	5.90 ± 1.10	6.95	61.99
No BDE	0.99	7.57 ± 0.18	6.21 ± 0.28	7.31	55.34
MC	0.98	11.09 ± 0.39	8.46 ± 0.98	9.96	110.46
No MC	0.99	7.57 ± 0.11	7.16 ± 0.19	8.43	63.82
Halo	0.95	10.43 ± 0.67	10.01 ± 1.72	11.78	122.86
No Halo	0.95	8.51 ± 0.59	6.24 ± 0.17	7.35	62.55

Table 12 Gaussian-fit parameters for the distribution of electric field [$E_{\max}$], central-peak value of $E_{\max}$ [x_c], width [w], full width at half maximum [w_c], and the product $x_c w_c$ during the passage of ICMEs with different structures/features.

ICME Structure	Gaussian-fit parameters for $E_{\max}$				
	R^2	x_c	w	w_c	$x_c w_c$
Shock	0.94	5.18 ± 0.26	4.07 ± 0.64	4.79	24.81
No Shock	0.99	3.87 ± 0.07	2.98 ± 0.09	3.51	13.58
BDE	0.93	4.70 ± 0.22	3.24 ± 0.66	3.81	17.91
No BDE	0.99	4.18 ± 0.05	2.84 ± 0.07	3.34	13.96
MC	0.92	5.35 ± 0.32	4.38 ± 0.73	5.16	27.61
No MC	0.98	4.27 ± 0.14	2.95 ± 0.24	5.03	21.48
Halo	0.91	5.25 ± 0.29	3.95 ± 0.75	6.18	32.44
No Halo	0.96	4.70 ± 0.18	3.65 ± 0.46	5.53	25.99

Appendix D

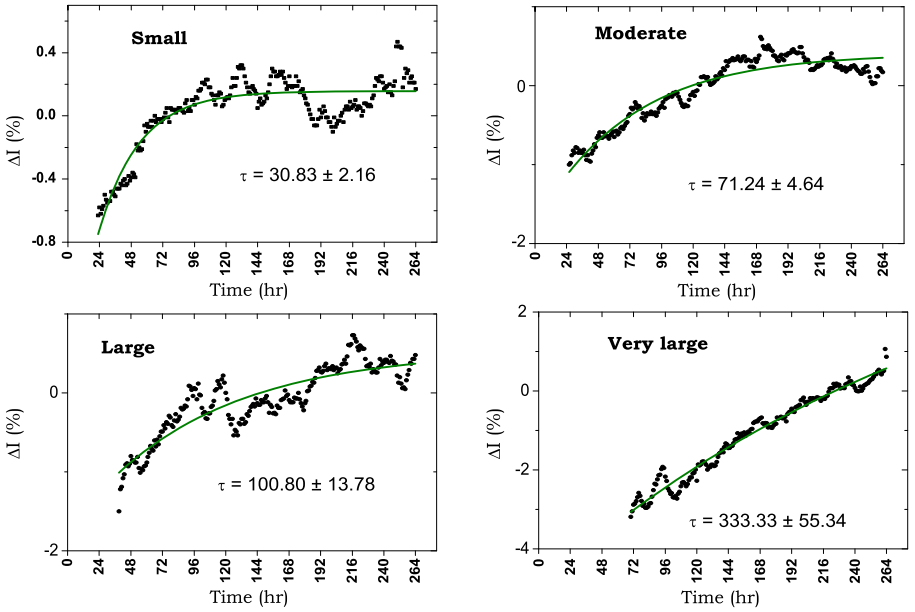

Figure 13 Exponential fit and characteristic recovery time [τ, hours] during recovery of GCR-intensity depressions due to ICMEs of different GCR-effectiveness.

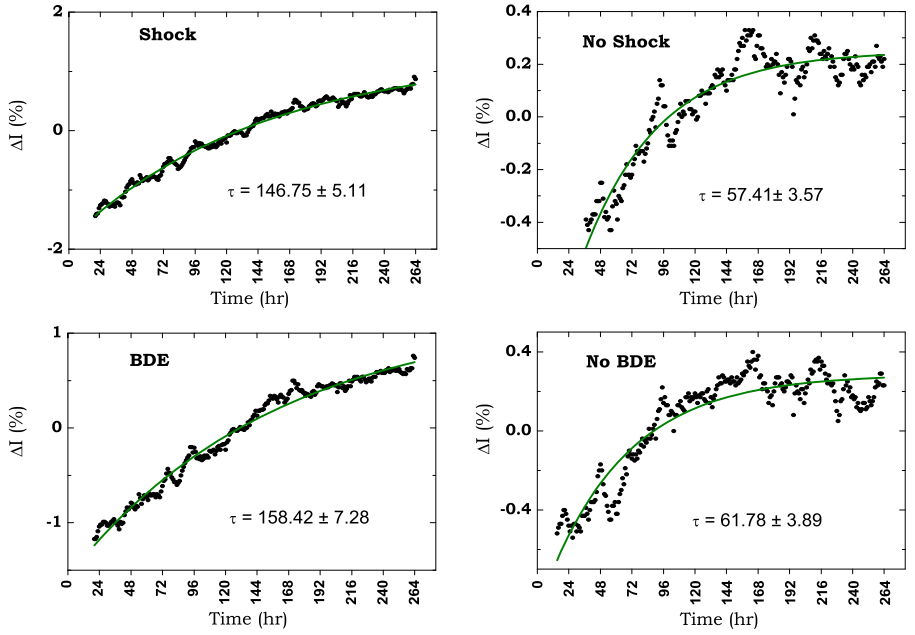

Figure 14 Exponential fit and characteristic recovery time [τ, hours] during recovery of GCR-intensity depressions due to ICMEs associated/not associated with shocks and bidirectional superthermal electron events (BDEs).

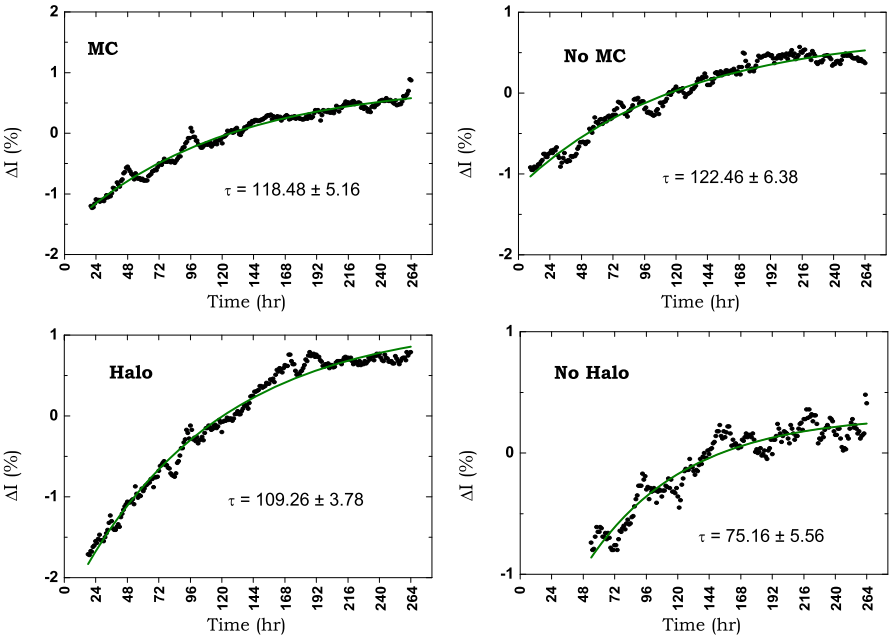

Figure 15 Exponential fit and characteristic recovery time [τ, hours] during recovery of GCR-intensity depressions due to ICMEs associated/not associated with magnetic cloud (MC) and halo CMEs.

References

Abbrescia, M., Aiola, S., Antolini, R., Avanzini, C., Baldini, F.R., Bencivenni, G., *et al.*: 2011, *Eur. Phys. J. Plus* **126**, 61.

Alves, M.V., Echer, E., Ganzalez, W.D.: 2011, *J. Atmos. Solar-Terr. Phys.* **73**, 1380.

Ananth, A.G., Venkatesan, D.: 1993, *Solar Phys.* **143**, 373. doi:10.1007/BF00646494.

Augusto, C.R.A., Kopkinen, V., Navia, C.E., Tsui, K.H., Shigueoka, H., Fauth, A.C., *et al.*: 2012, *Astrophys. J.* **759**, 143.

Babu, A., Antia, H.M., Dugad, S.R., Gupta, S.K., Hayashi, Y., Kawakami, S., Mohanty, P.K., Nonaka, T., Oshima, A., Subramanian, P.: 2013, *Astron. Astrophys.* **555**, A139.

Badruddin: 1998, *Planet. Space Sci.* **46**, 1015.

Badruddin: 2002, *Solar Phys.* **209**, 195. doi:10.1023/A:1020937324310.

Badruddin, Singh, Y.P.: 2009, *Planet. Space Sci.* **57**, 318.

Badruddin, Venkatesan, D., Zhu, B.Y.: 1991, *Solar Phys.* **134**, 203. doi:10.1007/BF00148748.

Badruddin, Yadav, R.S., Yadav, N.R.: 1986, *Solar Phys.* **105**, 413. doi:10.1007/BF00172057.

Badruddin, Yadav, R.S., Yadav, N.R., Agrawal, S.P.: 1985, In: Jones, F.C., Admas, J., Mason, G.M. (eds.) *Proc. 19th Int. Cosmic Ray Conf. La Jolla* **5**, 258. NASA conference Publication 2376.

Blanco, J.J., Catalan, E., Hidalgo, M.A., Medina, J., Garcia, O., Rodriguez-Pacheco, J.: 2013, *Solar Phys.* **284**, 167. doi:10.1007/s11207-013-0256-1.

Burlaga, L.F., Sittler, E., Mariani, F., Schwenn, R.: 1981, *J. Geophys. Res.* **86**, 6673.

Cane, H.V.: 1993, *J. Geophys. Res.* **98**, 3509.

Cane, H.V.: 2000, *Space Sci. Rev.* **93**, 55.

Cane, H.V., Richardson, I.G.: 2003, *J. Geophys. Res.* **108**, 1156.

Cane, H.V., Richardson, I.G., von Rosenvinge, T.T.: 1996, *J. Geophys. Res.* **101**, 21561.

Cane, H.V., Richardson, I.G., Wibberenz, G.: 1997, *J. Geophys. Res.* **102**, 7075.

Chree, C.: 1912, *Phil. Trans. Roy. Soc. London A* **212**, 75.

Dorotovic, I., Kudela, K., Lorenc, M., Rybansky, M.: 2008, *Solar Phys.* **250**, 339. doi:10.1007/s11207-008-9222-8.

Dumbovic, M., Vršnak, B., Calagovic, J., Karlica, M.: 2011, *Astron. Astrophys.* **531**, A91.

Dumbovic, M., Vršnak, B., Calagovic, J., Zupar, R.: 2012, *Astron. Astrophys.* **548**, A28.
Farrugia, C.J., Berdichevsky, D.B.: 2004, *Ann. Geophys.* **22**, 3679.
Forbush, S.E.: 1937, *Phys. Rev.* **31**, 1108.
Gopalswamy, N., Yashiro, S., Akiyama, S.: 2007, *J. Geophys. Res.* **112**, A06112.
Gopalswamy, N., Lara, A., Yashiro, S., Kaiser, M.L., Howard, R.A.: 2001, *J. Geophys. Res.* **106**, 29207.
Gosling, J.T.: 1990, In: Russel, C.T., Priest, E.R., Lee, L.C. (eds.) *Physics of Magnetic Flux Ropes*, *Geophys. Monogr.* **58**, AGU, Washington, 343.
Gosling, J.T.: 1996, *Annu. Rev. Astron. Astrophys.* **34**, 35.
Gosling, J.T., Baker, D.N., Bame, S.J., Feldman, W.C., Zwickl, R.D., Smith, E.J.: 1987, *J. Geophys. Res.* **92**, 8519.
Gupta, V., Badruddin: 2009, *Astrophys. Space Sci.* **312**, 185.
Iucci, N., Parisi, M., Signorini, C., Storini, M., Villoresi, G.: 1989, *Astron. Astrophys. Suppl.* **81**, 367.
Jian, L., Russel, C.T., Luhmann, J.G., Skoug, R.M.: 2006, *Solar Phys.* **239**, 393. doi:10.1007/s11207-006-0133-2.
Jordan, A.P., Spence, H.E., Blake, J.B., Shaul, D.N.A.: 2011, *J. Geophys. Res.* **116**, A11103.
Kahler, S.W., Reames, D.V.: 1991, *J. Geophys. Res.* **96**, 9419.
Kane, R.P.: 2010, *Ann. Geophys.* **28**, 479.
Klein, L.W., Burlaga, L.F.: 1982, *J. Geophys. Res.* **87**, 613.
Kudela, K.: 2012, In: Lazar, M. (ed.) *Exploring the Solar Wind* **13**, Intech, Rijeka, 285.
Kudela, K., Storini, M., Hofer, M.Y., Belov, A.: 2000, *Space Sci. Rev.* **93**, 153.
Lepping, R.P., Burlaga, L.F., Tsurutani, B.T., Ogilvie, K.W., Lazarus, A.J., Evans, D.S., Klein, L.W.: 1991, *J. Geophys. Res.* **96**, 9425.
LeRoux, J.A., Potgieter, M.S.: 1991, *Astron. Astrophys.* **243**, 531.
Liu, Y., Richardson, J.D., Belcher, J.W., Kasper, J.C., Skoug, R.M.: 2006, *J. Geophys. Res.* **111**, A09108.
Lockwood, J.A.: 1971, *Space Sci. Rev.* **12**, 658.
Lockwood, J.A., Webber, W.R., Debrunner, H.: 1991, *J. Geophys. Res.* **96**, 11587.
Marcz, F.: 1992, *Planet. Space Sci.* **40**, 979.
Mavromichalaki, H., Preka-Papadema, P., Liritzis, I., Petropoulos, B., Kurt, V.: 2003, *New Astron.* **8**, 777.
Modzelewska, R., Alania, M.V.: 2012, *Adv. Space Res.* **50**, 716.
Nagashima, K., Sakakibara, S., Fujimoto, K., Tatsuoka, R., Morishita, I.: 1990, *Nuovo Cimento* **13C**, 551.
Oh, S.Y., Yi, Y.: 2009, *J. Geophys. Res.* **114**, A11102.
Oh, S.Y., Yi, Y.: 2012, *Solar Phys.* **280**, 197. doi:10.1007/s11207-012-0053-2.
Oh, S.Y., Yi, Y., Kim, Y.H.: 2008, *J. Geophys. Res.* **113**, A01103.
Quenby, J.J., Mulligan, T., Blake, J.B., Mazur, J.E., Shaul, D.: 2008, *J. Geophys. Res.* **113**, A10102.
Rao, U.R.: 1972, *Space Sci. Rev.* **12**, 719.
Richardson, I.G., Cane, H.V.: 2010, *Solar Phys.* **264**, 189. doi:10.1007/s11207-010-9568-6.
Richardson, I.G., Cane, H.V.: 2011, *Solar Phys.* **270**, 609. doi:10.1007/s11207-011-9774-x.
Reames, D.V., Kahler, S.W., Tylka, A.J.: 2009, *Astrophys. J. Lett.* **700**, L196.
Sabbah, I., Kudela, K.: 2012, *J. Geophys. Res.* **116**, A041303.
Simpson, J.A.: 1954, *Phys. Rev.* **94**, 426.
Singh, Y.P., Badruddin: 2006, *J. Atmos. Solar-Terr. Phys.* **68**, 803.
Singh, Y.P., Badruddin: 2007, *J. Geophys. Res.* **112**, A02101.
Subramanian, P., Antia, H.M., Dugad, S.R., Goswami, U.D., Gupta, S.K., Hayashi, Y., *et al.*: 2009, *Astron. Astrophys.* **494**, 1107.
Usoskin, I.G., Braun, I., Gladysheva, G.G., Horandel, J.R., Jamsen, T., Kovaltsov, G.A., Starodubtsev, S.A.: 2008, *J. Geophys. Res.* **113**, A07102.
Venkatesan, D., Badruddin: 1990, *Space Sci. Rev.* **52**, 121.
Venkatesan, D., Badruddin, Ananth, A.G., Pillai, S.: 1992, *Solar Phys.* **137**, 345. doi:10.1007/BF00161855.
Wawrzynczak, A., Alania, M.V.: 2010, *Adv. Space Res.* **45**, 622.
Wibberenz, G., LeRoux, J.A., Potgieter, M.S., Bieber, J.W.: 1998, *Space Sci. Rev.* **83**, 309.
Yu, X.X., Lu, H., Le, G.M., Shi, F.: 2010, *Solar Phys.* **263**, 223. doi:10.1007/s11207-010-9522-7.
Zhang, G., Burlaga, L.F.: 1988, *J. Geophys. Res.* **93**, 2511.
Zhang, J., Richardson, I.G., Webb, D.F., Gopalswamy, N., Huttunen, E., Kasper, J.C., Nitta, N.V., Poomvises, W., Thomson, B.J., Wu, C.C., Yashiro, S., Zhukov, A.N.: 2007, *J. Geophys. Res.* **112**, A10102.